Analysis of Mach-Zehnder Interferometers

KOMAL GUPTA[1,*]

[1]*Institute of Photonics Technologies, National Tsing Hua University, Hsinchu, Taiwan 300*
*komalgupta@gapp.nthu.edu.tw

Abstract: This report presents a study of a Mach-Zehnder Interferometer (MZI) on a silicon-on-insulator (SOI) platform. The investigation includes numerical analysis of waveguide propagation modes, variations in effective index, and group index. Additionally, the simulated and experimental fitted transfer function, transmission characteristics, corner analysis of device dimensions, group index variations, and free spectral range (FSR) calculations are examined for an imbalanced MZI.

1. Introduction

Integrated photonic devices based on silicon-on-insulator (SOI) platforms have gained significant attention due to their compact footprint, CMOS compatibility, and high-performance optical characteristics [1-3]. Among these devices, Mach-Zehnder interferometers (MZIs) are widely used for sensing, modulation, and filtering applications due to their precise phase-dependent interference. However, optimizing MZI performance requires careful analysis of waveguide properties, including propagation modes, effective index, and group index, as well as the spectral response under imbalanced path conditions.

This work investigates an SOI-based MZI, examining its modal behavior and refractive index variations to understand their influence on device functionality. Through simulations, the transfer function, transmission spectrum, and free spectral range (FSR) for different path length imbalances was evaluated, providing insights into design trade-offs for targeted applications. Additionally, a mask layout of fabricated devices and their experimental validation is presented.

2. Theory

The operation of a Mach-Zehnder interferometer (MZI) on a silicon-on-insulator (SOI) platform can be comprehensively described through electromagnetic wave propagation theory [4]. Figure. 1 shows a schematic of a simple MZI. When light enters the input Y-junction, the electric field E_{in} is equally divided into two arms, expressed as $E_1 = E_{in}e^{(i\beta_1 L_1)}/\sqrt{2}$ and $E_2 = E_{in}e^{(i\beta_2 L_2)}/\sqrt{2}$, where $\beta = 2\pi n_{eff}/\lambda$ represents the propagation constant, n_{eff} is the waveguide's effective refractive index, and L_1 and L_2 denote the lengths of the two interferometer arms. The path length difference is equally divided into two arms, expressed as $\Delta L = L_2 - L_1$ introduces a critical phase shift $\Delta\phi = \beta\Delta L$ between the two arms, which fundamentally determines the interferometer's behavior. For a Y-branch splitter, $E_1 = E_2 = E_{in}/\sqrt{2}$.
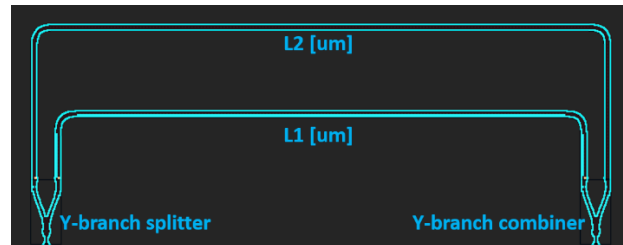

Figure 1. Schematic of a simple MZI.

The output of the Y- branch combiner for a lossless imbalanced MZI with $\beta_1 = \beta_2 = \beta$ is given by E_o (equation 1) and the corresponding transfer function is given by I_o (equation 2).

$$E_o = \frac{E_{in}}{2} \left(e^{(-i\beta_1 L_1)} + e^{(-i\beta_2 L_2)} \right) \tag{1}$$

$$I_o = \frac{I_{in}}{2} \left[1 + \cos(\beta \Delta L) \right] \tag{2}$$

The above relationship reveals the periodic nature of the MZI's transmission function, where constructive and destructive interference occur at specific phase differences. The periodicity of this interference pattern is characterized by the free spectral range (FSR), given by

$$FSR = \frac{\lambda^2}{n_g(\lambda)\,\Delta L} \tag{3}$$

where n_g is the group index defined by

$$n_g(\lambda) = n_{eff}(\lambda) - \lambda \frac{dn_{eff}(\lambda)}{d\lambda} \tag{4}$$

which accounts for waveguide dispersion effects. The group index plays a crucial role in determining the wavelength-dependent performance of the device, particularly in broadband applications. Practical implementations consider propagation losses, which modify the ideal transfer function. When accounting for attenuation coefficient α, the transmission becomes

$$I_o = \frac{I_{in}}{4} \left[e^{(-i\alpha_1 L_1)} + e^{(-i\alpha_2 L_2)} + 2e^{-\frac{\alpha_1 L_1 + \alpha_2 L_2}{2}} \cos(\beta \Delta L) \right] \tag{5}$$

This more complete expression demonstrates how fabrication imperfections and material losses influence the device's performance. The effective index $n_{eff}(\lambda)$, which depends on the waveguide geometry and material properties, can be determined through numerical mode-solving techniques, while the group index n_g provides insight into the device's dispersion characteristics. Together, these parameters enable precise engineering of the MZI's spectral response for applications in optical filtering, modulation, and sensing. The theoretical framework presented here forms the basic foundation for designing imbalanced MZI devices in SOI platforms.

3. Modeling and Simulations

3.1 Waveguide Modeling

The strip waveguide structure was simulated using Lumerical MODE Solver, with cross-sectional dimensions of 220 nm (height) × 550 nm (width) which is a standard specification adopted by major silicon photonics foundries. Modal analysis was conducted at the wavelength of 1550 nm to characterize the guided modes. Figure 2(a) shows the simulated transverse electric (TE) mode profile, while Figure 2(b) shows the corresponding transverse magnetic (TM) mode distribution, clearly illustrating the distinct field confinement characteristics for each polarization state.
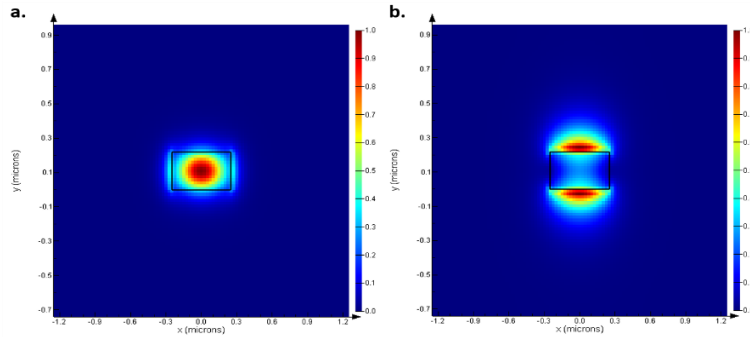

Figure 2. Simulated mode profiles (a) TE and (b) TM.

The wavelength-dependent characteristics of the fundamental TE mode were investigated through systematic parameter sweeps. Figure 3 presents the spectral analysis results, where (a) shows the wavelength dependence of both real and imaginary components of the effective refractive index, while (b) displays the corresponding group index variations across the 1500-1600 nm wavelength range. The real part of the effective index exhibits characteristic normal dispersion behavior, decreasing monotonically with increasing wavelength, while the imaginary component reveals wavelength-dependent propagation losses. The group index demonstrates a gradual reduction across the spectrum, consistent with the known dispersion properties of silicon waveguides in this spectral region.
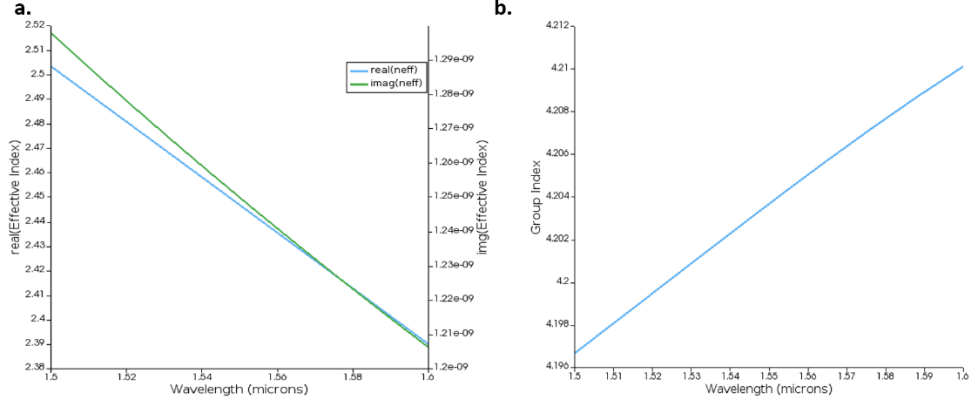

Figure 3. Wavelength dependence of (a) effective index and (b) group index for TE mode.

For designing the compact waveguide model supporting the TE mode, the wavelength dependence of the effective index was analytically represented through Taylor series expansion (equation 6), with the corresponding coefficients systematically determined. The fitted equation takes the form

$$n_{eff}(\lambda) = n_0 + n_1(\lambda - \lambda_0) + n_3(\lambda - \lambda_0)^2 \tag{6}$$

$$\Rightarrow n_{eff}(\lambda) = 2.44682 - 1.13339(\lambda - \lambda_0) - 0.0439(\lambda - \lambda_0)^2 \tag{7}$$

where n_0 represents the effective index at the central wavelength $\lambda_0 = 1550$ nm, and the higher-order terms capture the dispersion characteristics. Figure 4 demonstrates excellent agreement between the numerically calculated effective indices (discrete points) and the Taylor series approximation (solid curve), validating the accuracy of this compact model.
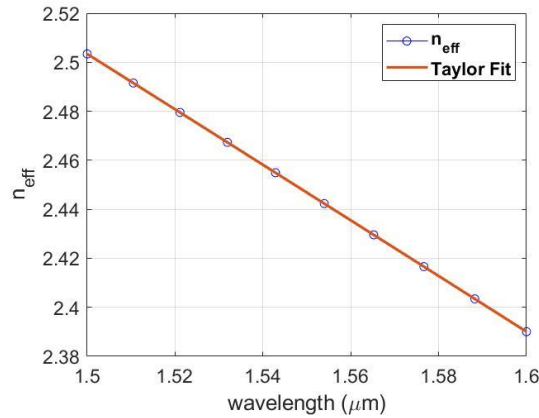

Figure 4. Compact model of the waveguide for TE mode.

The compact waveguide model was employed to numerically simulate the transfer function of an imbalanced MZI through MATLAB. Figure 5 presents the comprehensive simulation results. Figure 5 (a) and (b) depict the spectral transmission characteristics in linear scale and logarithmic (dB) scale respectively, revealing the periodic wavelength-dependent interference pattern. The complementary analysis in (c) and (d) demonstrates the MZI's transmission response as a function of path length difference (ΔL) at the design wavelength of 1550 nm, showing the expected sinusoidal dependence of the interferometric output on the optical phase difference. The 2-D transmission map in (e) shows that as the differential arm length ΔL is increased from 50 µm to 250 µm the interference fringes crowd together, so the FSR in wavelength shrinks from a few nm to below 1 nm, exactly following the expected $1/\Delta L$
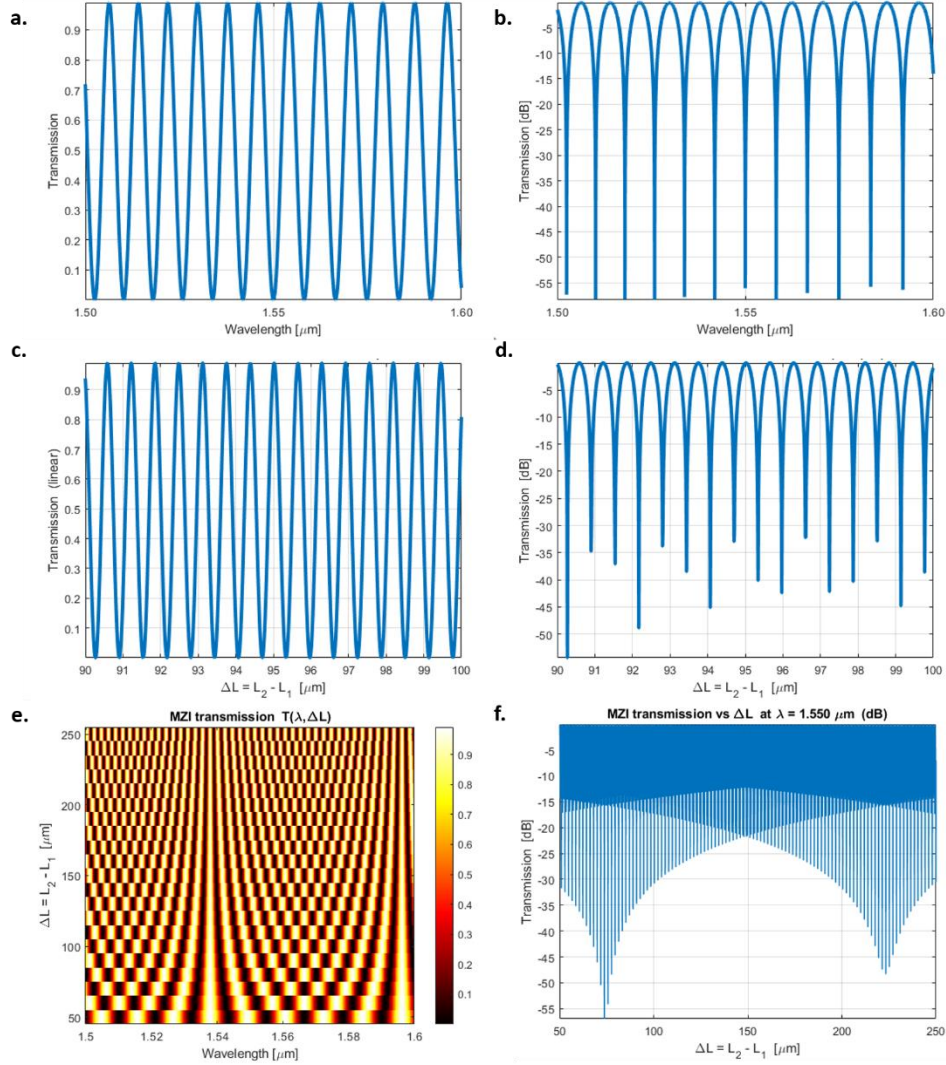

Figure 5. MZI transmission characteristics: Wavelength dependence (a) linear and (b) dB scale. ΔL dependence at 1550 nm (c) linear scale and (d) dB scale. (e) Linear transmission as a function of long range ΔL and wavelength and (f) Transmission in dB dependence on ΔL for the operational wavelength of 1550nm.

behavior of an MZI. At the design wavelength $\lambda = 1.550$ µm the ΔL-scan exhibits a comb of narrow peaks separated by ≈ 1.55 µm and flanked by deep nulls >50 dB down, demonstrating

high phase sensitivity and excellent 50/50 coupler balance as shown in (f). Together, these features confirm that the device can deliver narrow-band filtering and precision phase sensing with large extinction ratios over a broad range of arm imbalances.

3.2 MZI Modeling, Simulations, and Experiments

The MZI structure incorporating Y-branches (as splitter and combiner) with varying path length differences (ΔL) was simulated using Lumerical INTERCONNECT to systematically investigate its spectral characteristics. The consistent waveguide geometry (220 nm × 550 nm) and single-mode operation at 1550 nm ensures comparable modal properties across all designs, enabling clear observation of how ΔL modification affects both the spectral periodicity (FSR) and insertion loss characteristics of the MZI devices.

Following simulation, the proposed MZI designs were translated into fabrication-ready layouts using KLayout. Figure 6 presents the complete schematic of the four MZI implementations, incorporating specific design features to facilitate automated optical testing. The layout incorporated two critical constraints to ensure compatibility with the measurement setup: (1) all TE grating couplers were oriented toward the right side of the chip to eliminate the need for rotational alignment during testing, and (2) a fixed 127 μm pitch was maintained for both input and output grating couplers to precisely match the fiber array configuration of the automated probe station.

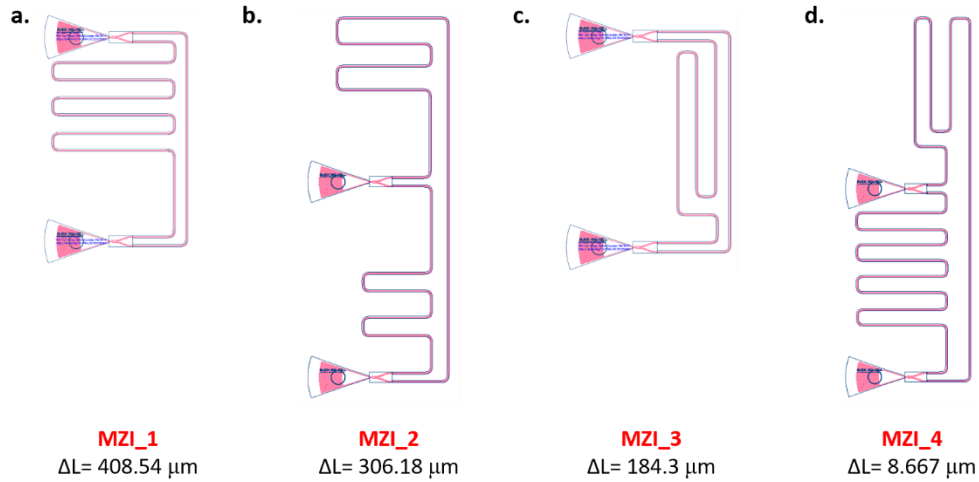|			
MZI_1	**MZI_2**	**MZI_3**	**MZI_4**
ΔL= 408.54 μm	ΔL= 306.18 μm	ΔL= 184.3 μm	ΔL= 8.667 μm

Figure 6. Proposed layout of different MZI(s).

The proposed devices were fabricated using the NanoSOI MPW fabrication process by Applied Nanotools Inc. which is based on direct-write 100 keV electron beam lithography technology. Silicon-on-insulator wafers of 200 mm diameter, 220 nm device thickness and 2 μm buffer oxide thickness are used as the base material for the fabrication. To characterize the devices, a custom-built automated test setup [4, 8] with automated control software written in Python was used [5]. An Agilent 81600B tunable laser was used as the input source and Agilent 81635A optical power sensors as the output detectors. The wavelength was swept from 1500 to 1600

nm in 10 pm steps. A polarization maintaining (PM) fiber was used to maintain the polarization state of the light, to couple the TE polarization into the grating couplers [6]. A 90º rotation was used to inject light into the TM grating couplers [6]. A polarization maintaining fiber array was used to couple light in/out of the chip [7].

Measurement Data Analysis

The experimental results were further processed to extract key device parameters, visualize the data clearly, and compare the measurements with theoretical predictions. To ensure accuracy, the raw experimental spectra were first baseline-corrected and calibrated by fitting a low-order polynomial to model the baseline, which was then subtracted from the measured data over the wavelength range of interest. The corrected spectrum was subsequently analyzed using curve-fitting techniques, where peaks in the MZI spectrum were identified using a peak-finding algorithm. From this fitted spectrum, the FSR was determined, and the corresponding group index was extracted. These extracted parameters were then compared with theoretical models and numerical simulations to validate the performance of the fabricated device. Figure 7 illustrates the complete analysis workflow. Figure 7(a) shows the raw experimental data, 7(b and c) presents the baseline-corrected spectrum, 7(d) displays the fitted peaks obtained using the find peaks function, 7(e) shows the FSR derived from the data, 7(f) finds starting point for curve fitting MZI, using the group index data, 7(g) provides the initial fitting parameters, 7(h) shows the final fitted model of the MZI response, and Figure 7(i) depicts the variation of the extracted group index based on the corner analysis. Figure 7(j) shows the comparison of experiments vs simulated response of the MZI. This systematic approach ensured that the experimental data were precisely processed and that the derived device parameters aligned well with theoretical expectations.
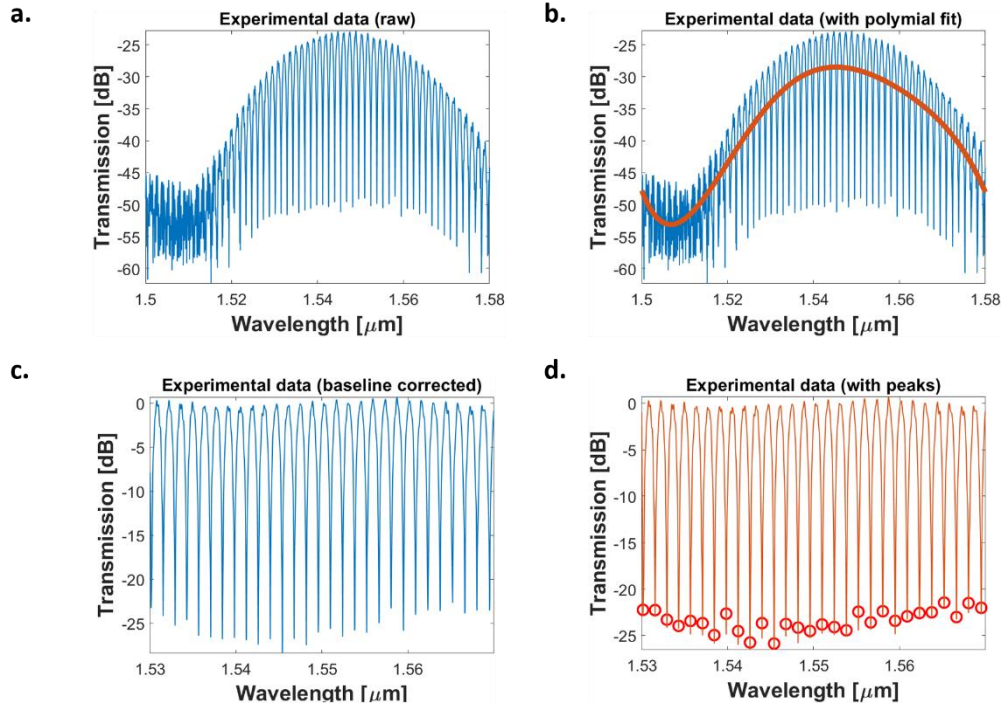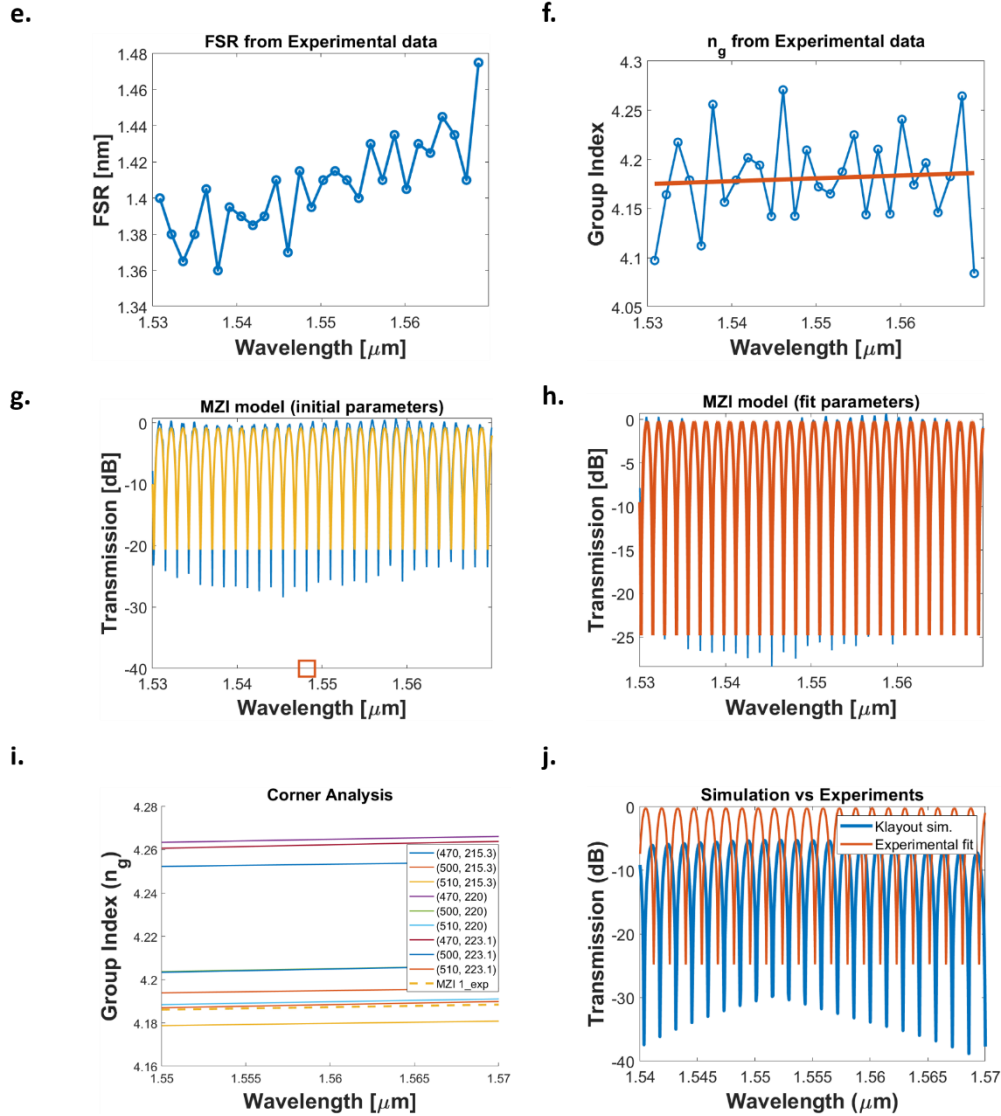
Figure 7. Shows complete analysis workflow for the MZI data: (a) raw experimental data, (b–c) baseline-corrected spectrum, (d) fitted peaks using findpeaks in MATLAB, (e) extracted FSR, (f) group index data used to find initial fitting points, (g) initial fitting parameters, (h) final fitted MZI model, (i) variation of extracted group index from corner analysis, and (j) comparison of experimental and simulated MZI responses.

The same methodology was applied to analyze the devices MZI_2 and MZI_3. Figures 8(a) and 8(b) present the fitted parameters for MZI_2, including the comparison with simulations and the corresponding corner analysis. Figures 8(c) and 8(d) show the fitted parameters for MZI_3 alongside its simulated response and corner analysis.

However, for MZI_4, shown in Figure 8(e), the path length difference was very small, resulting in a large FSR of approximately 40 nm. This FSR exceeded the measurement range of the experimental setup, making it impossible to extract the device parameters reliably.
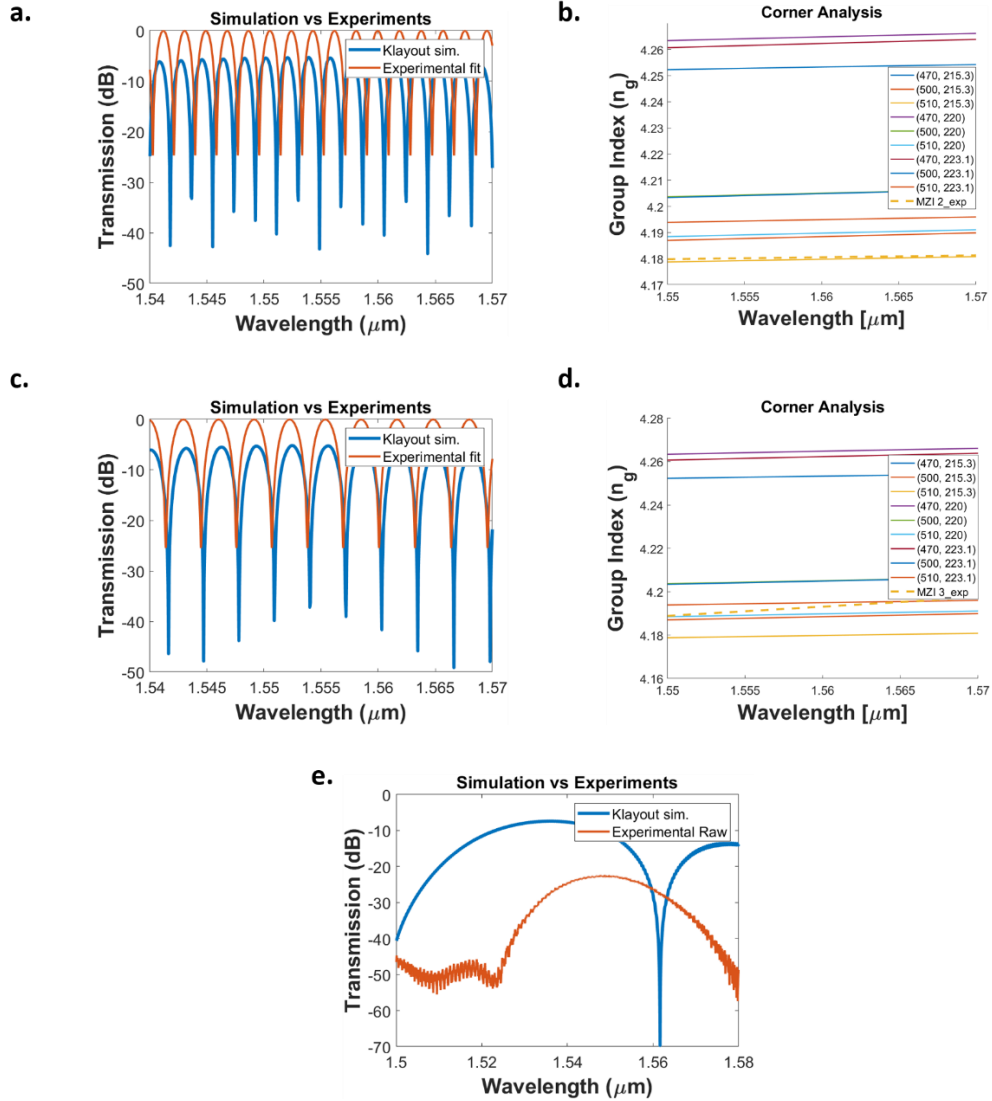
Figure 8. Analysis of additional MZI devices: (a–b) fitted parameters for MZI_2, including comparison with simulations and corner analysis; (c–d) fitted parameters for MZI_3 with corresponding simulation and corner analysis; (e) measured spectrum of MZI_4, which shows a large FSR due to a minimal path length difference, preventing parameter extraction.

From the MZI fitting, the effective index parameters (n_{eff}) were extracted according to Equation (7), along with the goodness of fit (r^2) for each device. The simulated FSR values obtained from KLayout-Interconnect were systematically compared with the fitted MZI responses to validate the analytical model. Table 1 summarizes the MZI fitting parameters, while Table 2 presents a comparative study of the FSR and group index, demonstrating excellent agreement between the predicted and simulated results across different path length differences (ΔL). This verification confirms the accuracy of both the waveguide dispersion model and the MZI transfer function implementation.

Table 1. MZI fitting parameters

Device Name	$n_{eff}(\lambda)$	r^2
MZI_1	$2.3968 - 1.1556(\lambda - \lambda_0) - 0.0376(\lambda - \lambda_0)^2$	0.98788
MZI_2	$2.3999 - 1.1538(\lambda - \lambda_0) - 0.0236(\lambda - \lambda_0)^2$	0.99384
MZI_3	$2.3973 - 1.1571(\lambda - \lambda_0) - 0.1235(\lambda - \lambda_0)^2$	0.9935

Table 2. FSR for different ΔL

Device name	ΔL (μm)	FSR Experimental	FSR Simulated	n_g Experimental	n_g Simulated
MZI_1	408.54	1.41 nm	1.399 nm	4.1859	4.190
MZI_2	306.18	1.885 nm	1.85 nm	4.1792	4.1899
MZI_3	184.3	3.115 nm	3.04 nm	4.1888	4.19
MZI_4	8.667	(beyond the measurements limit)	40.94 nm	-	4.189

Michelson Interferometer

The Michelson interferometer is a widely used optical configuration that splits a beam into two arms, reflects them back using mirrors, and then recombines them to produce an interference pattern that depends on the path length difference between the arms. After studying the impact of varying path length differences in the MZI devices, I further analyzed the data for both balanced and imbalanced Michelson interferometers to investigate their interference characteristics and parameter extraction. Figure 9 shows the KLayout schematic of the fabricated Michelson interferometers: (a) the balanced interferometer and (b) the imbalanced interferometer.
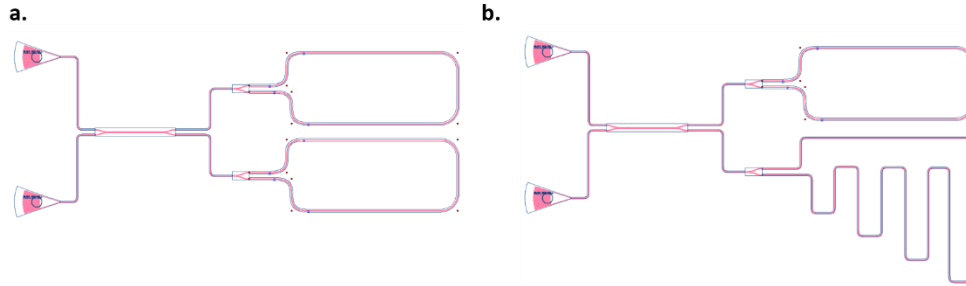

Figure 9. KLayout schematics of the fabricated Michelson interferometers: (a) balanced configuration and (b) imbalanced configuration.

The impact of the balanced and imbalanced Michelson interferometers can be seen in Figure 10. Figure 10(a) shows the experimental and simulated spectra for the balanced MI, which has an FSR of 48 nm — a value that exceeds the measurement range, making parameter extraction infeasible.
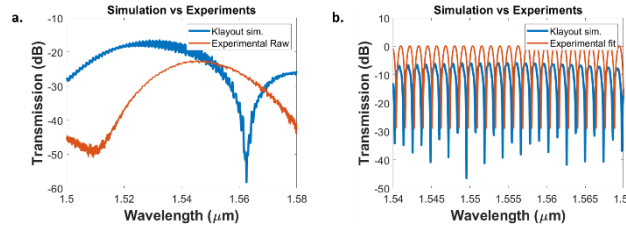

Figure 10. Experimental and simulated results for the Michelson interferometers: (a) balanced configuration showing an FSR beyond the measurable range; (b) comparison of fitted and simulated transmission for the imbalanced configuration.

In contrast, for the imbalanced configuration, the simulated and experimentally extracted FSR is approximately 1.15 nm, with the experimental group index determined to be 4.172. The fitted effective index is $n_{eff}(\lambda) = 2.3974 - 1.1494(\lambda - \lambda_0) - 0.0593(\lambda - \lambda_0)^2$. Figure 10(b) compares the experimentally fitted and simulated transmission spectra for the imbalanced Michelson interferometer.

4. Conclusions

This report presents the design, fabrication, and detailed analysis of multiple Mach–Zehnder interferometers (MZIs) and Michelson interferometers (MIs) implemented using silicon strip waveguides with varying path length differences. The study systematically investigates the waveguide modal characteristics, effective index dispersion, and spectral response of both balanced and imbalanced configurations. Using numerical simulations and theoretical modeling, the MZI designs were optimized to achieve target free spectral ranges (FSRs) and were validated through experimental measurements and fitting procedures that demonstrate excellent agreement with the analytical models. The impact of path length variation on the interference spectra was confirmed for both MZI and MI structures, highlighting that large FSR values may exceed practical measurement limits for highly balanced designs. The fabricated layouts include test-optimized features such as right-oriented grating couplers and a 127 μm fiber pitch to enable automated optical characterization. Overall, the results confirm the reliability of the dispersion model and transfer function implementation, providing a robust framework for the design and characterization of silicon photonic interferometers.

References

1. H. Subbaraman, X. C. Xu, A. Hosseini et al., "Recent advances in silicon-based passive and active optical interconnects," Opt Express **23**, 2487-2510 (2015).
2. Michal Lipson, "Guiding, Modulating, and Emitting Light on Silicon-Challenges and Opportunities," J. Lightwave Technol. 23, 4222- (2005)
3. Bogaerts, W., De Heyn, P., Van Vaerenbergh, T., De Vos, K., Kumar Selvaraja, S., Claes, T., Dumon, P., Bienstman, P., Van Thourhout, D. and Baets, R. (2012), Silicon microring resonators. Laser & Photon. Rev., 6: 47-73.
4. Chrostowski L, Hochberg M. Silicon Photonics Design: From Devices to Systems. Cambridge University Press; 2015.
5. http://siepic.ubc.ca/probestation, using Python code developed by Michael Caverley.
6. Yun Wang, Xu Wang, Jonas Flueckiger, Han Yun, Wei Shi, Richard Bojko, Nicolas A. F. Jaeger, Lukas Chrostowski, "Focusing sub-wavelength grating couplers with low back reflections for rapid prototyping of silicon photonic circuits", Optics Express Vol. 22, Issue 17, pp. 20652-20662 (2014) doi: 10.1364/OE.22.020652
7. www.plcconnections.com, PLC Connections, Columbus OH, USA.
8. http://mapleleafphotonics.com, Maple Leaf Photonics, Seattle WA, USA.